Journal of Materials Science & Technology 102 (2022) 36–45

Contents lists available at ScienceDirect

Journal of Materials Science & Technology

journal homepage: www.elsevier.com/locate/jmst

Research Article

Manipulating internal flow units toward favorable plasticity in Zr-based bulk-metallic glasses by hydrogenation

Fuyu Dong[a], Yuexin Chu[a], Mengyuan He[a,b], Yue Zhang[a,*], Weidong Li[c,*], Peter K. Liaw[c,*], Binbin Wang[d], Liangshun Luo[d], Yanqing Su[d], Robert O. Ritchie[e], Xiaoguang Yuan[a]

[a] School of Materials Science and Engineering, Shenyang University of Technology, Shenyang, China
[b] School of Materials Science and Engineering, Northeastern University, Shenyang, China
[c] Department of Materials Science and Engineering, The University of Tennessee, Knoxville, TN, USA
[d] School of Materials Science and Engineering, Harbin Institute of Technology, Harbin, China
[e] Department of Materials Science and Engineering, University of California, Berkeley, CA, 94720, USA

ARTICLE INFO

Article history:
Received 15 March 2021
Revised 5 April 2021
Accepted 10 April 2021
Available online 17 June 2021

Keywords:
Bulk-metallic glass
Plasma-assisted hydrogenation
Nanoindentation
Internal flow unit
Serrations
Nano-scale creep

ABSTRACT

This work intends to manipulate the internal flow units in $Zr_{55}Cu_{30}Ni_5Al_{10}$ bulk-metallic glasses (BMGs) through plasma-assisted hydrogenation to generate a positive microalloying effect on plasticity. Based on the cooperative shear model theory, serration-flow statistics during nanoindentation loading and creep tests during the holding stage were used to analyze the influence of hydrogen on the behavior of flow units in BMGs. Experimental observations showed that the hydrogen in the $Zr_{55}Cu_{30}Ni_5Al_{10}$ BMGs caused mechanical softening, plasticity improvement, and structural relaxation. Analysis also showed that the average volume, size, and activation energy of internal flow units in the BMGs all increased as a result of the increase in the hydrogen content. The hydrogenation in the BMGs was found to lead to a proliferation of shear bands, which promoted plasticity. The aggregation of these internal flow units reduced the stress required for plastic deformation through shear bands, ultimately causing softening and structural relaxation.

© 2021 Published by Elsevier Ltd on behalf of Chinese Society for Metals.

1. Introduction

The effect on hydrogen on metallic glasses (MGs) has been a popular topic for materials scientists and engineers for many decades because such materials have potential applications for efficient hydrogen (H) storage and separation [1-3]. In addition to these possibilities, scientific interest has been motivated by observations that hydrogen additions can modify the glass-forming ability (GFA) and result in improved ductility [4-8]. To achieve such beneficial effects, we recently presented a processing route for introducing H into MGs via plasma-assisted hydrogenation [9]. Such hydrogenation offers new strategies for the alloy design of MGs. Moreover, it provides a potential method for resolving the problem that high glass-forming ability and ductility in MGs are often mutually exclusive properties. Although some studies have addressed the mechanical behavior of hydrogenated MGs [10-13], few have examined the influence of hydrogen on deformation mechanisms in MGs, particularly in bulk-metallic glasses (BMGs) with a high Zr content, *i.e.*, those with $\geq$ 50 atomic percent (at.%) Zr. Indeed, the precise deformation mechanisms in hydrogenated MGs are still unclear and in many respects somewhat controversial.

Current research has revealed close correlations between the internal flow units in MGs and their deformation mechanisms [14-16]. In MGs, the cooperative motions of atoms and free volumes, which act as internal flow units, derive from structural heterogeneities or "potential flow defects" [14]. Compared with other atoms in amorphous alloys, atoms in internal flow units have low elastic modulus, low strength, loose atomic arrangement, high energy, and large atomic mobility. Accordingly, these regions are often referred to as "soft zones" or "liquid-like zones" [17-19]. These soft zones, embedded in rigid amorphous substrates, cannot store elastic energy. Under the action of external temperatures and stresses, they exhibit rheological characteristics and can dissipate energy, which in turn affect the structures and properties of MGs. Flow units have been described using several phenomenological models [20-22], which are mainly based on three mechanisms: the local atomic jump, shear-transformation zone (STZ), and cooperative shearing mechanisms. Internal flow units comprise another degree of disorder in the disordered system of BMGs, which need to be resolved both spatially and temporally. Their struc-

* Corresponding authors.
E-mail addresses: yuezhang@sut.edu.cn (Y. Zhang), wli20@vols.utk.edu (W. Li), pliaw@utk.edu (P.K. Liaw).

https://doi.org/10.1016/j.jmst.2021.04.037
1005-0302/© 2021 Published by Elsevier Ltd on behalf of Chinese Society for Metals.

turally complex nature derives from their amorphous structures, rendering them challenging to measure using existing analytical techniques [23, 24]. As it is difficult to accurately track structural evolution experimentally, much research on this topic has resorted to molecular dynamics simulations [25]. However, the limitations of the computational power make molecular dynamics only feasible for simulating very simple systems, such as binary or ternary alloys. Recently, on the basis of the cooperative shear model presented by Johnson and Samwer [22], Pan et al. [26] have proposed an experimental method for characterizing the STZ-volume, which allows the calculation of the experimental variation of internal flow units below the glass-transition temperature, T_g.

For hydrogenated MGs, the influence of hydrogen on their mechanical behavior has become somewhat controversial. Some studies have found that internal flow units and shear yield strengths (τ_{max}) of Ni–Nb–Zr hydrogenated MG ribbons are affected by the Zr content [27, 28]. Specifically, a low Zr content induces hydrogen-induced softening, whereas a high Zr content causes hydrogen-induced hardening. However, the results of other investigations have revealed that after hydrogenation, the high-Zr-content MGs clearly soften and exhibit improved plasticity [6, 9, 29, 30]. These contrasting effects are presumed to be closely related to the existing form and content of the H in MGs. Accordingly, motivated by the previous research, we propose in the present study to induce positive microalloying effects by manipulating the amount of internal flow units in Zr-based BMGs through plasma-assisted hydrogenation. We performed nanoindentation and hardness experiments to characterize the resulting mechanical behavior of the hydrogenated BMGs. Based on the cooperative shear model theory (CSM), serration-flow statistics and creep tests based on the strain-rate sensitivity were used to analyze the influence of hydrogen on the behavior of flow units in MGs during the loading and holding stages of nanoindentation tests in an attempt to further bridge the relationship between the deformation mechanisms and flow units in hydrogenated MGs.

2. Experimental

The precursor $Zr_{55}Cu_{30}Ni_5Al_{10}$ alloys were produced by mixing high-purity metals [≥ 99.9% weight percent, wt.%] in a Ti-gettered H_2-Ar atmosphere (three conditions, i.e., Ar/H_2 = 100, 90/10, and 85/15, by volume) using a plasma-assisted hydrogenation method in a water-cooled copper crucible [9]. The heat input was consistent with chemical homogeneity ensured by remelting the ingots five times. Using such a process, 3-mm-diameter BMG rods were produced by in situ suction casting in a water-cooled copper mold. A water-cooled diamond saw was used to cut rod specimens of 3 mm in diameter and 6 mm in length from the BMG ingots. The upper and lower parallel faces were ground to a roughness of less than 10 μm, with one surface mechanically polished to a mirror finish. These glass structures were analyzed using X-ray diffractions with Cu-K_α radiation, scanned from 20 to 100° at a scanning speed of 5°/min. Hydrogen concentrations were measured using a LECO ROH600 oxygen-H analyzer (90/10% Ar/H_2, 0.021 wt.% and 85/15% Ar/H_2, 0.026 wt.%), manufactured by LECO Corp. (St. Joseph, MI, USA). Thermal properties of the samples were characterized using differential scanning calorimetry (DSC, NETZSCH STA-409) with a constant heating rate of 20 K/min.

An Agilent Nano Indenter G200 (Agilent Technologies, Inc., Santa Clara, CA, USA) with a Berkovich diamond indenter was employed to carry out load-controlled nanoindentation measurements at room temperature. The displacement and load resolutions of the machine were, respectively, less than 0.01 nm and 50 nN, respectively. Before testing, the instrument was calibrated using the standard fused silicon to ensure thermal stability for at least 30 min., until the thermal drift was below 0.05 nm•s^{-1}. All nanoindentation experiments were loaded to 150 mN at a 1 mN/s loading rate. Creep behavior was studied by holding the maximum load for 250 s once reached. Finally, the loads were decreased at a rate of 1 mN/s. The contact stiffness was accurately measured by dynamic nanoindentation technique (DNT) [31-33] with a frequency of 45 Hz and displacement amplitude of 2 nm. Each testing condition was repeated at least four times to ensure repeatability. The material volumes used in our nanoindentation tests were cut out of the central region of the ingots, and the mechanical properties within such confined volumes are believed to be homogeneous. Therefore, an appreciable difference is not expected between performing 4 tests and many tests at a large spatial spread. Furthermore, our statistical analysis was performed on serrations. Although we conducted 4 tests in each condition, hundreds of serrations extracted from each test can still ensure the validity and quality of our statistical analysis. The Vickers hardness of the samples was examined using a HVS-5 digital low-load Vickers hardness tester (SGtest Instruments, Negeri Sembilan Darul Khusus, Malaysia) with a loading force of 1000 gf and a holding duration of 10 s. The morphology of the indents after the hardness tests were imaged, using a Hitachi S-3400 N scanning electron microscope (SEM) to identify the salient deformation mechanisms.

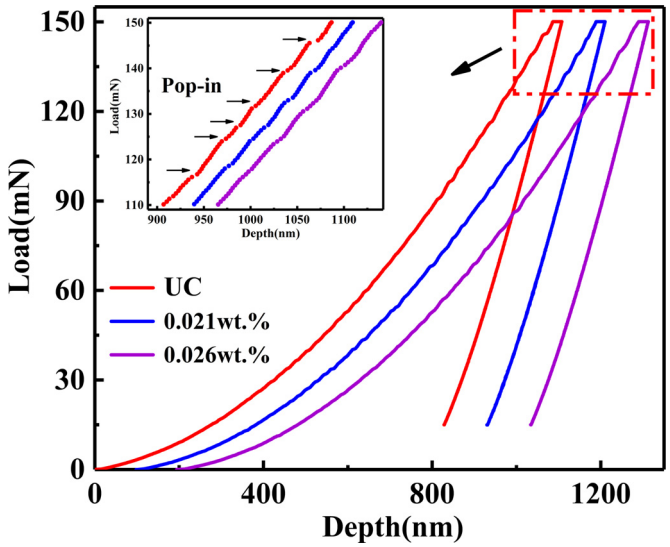

Fig. 1. Representative nanoindentation load-displacement (*P-h*) curves of the $Zr_{55}Cu_{30}Ni_5Al_{10}$ BMGs with various H contents. The inset shows different pop-in phenomena at the end of loading. The term UC refers to BMGs with uncharged H.

3. Results

3.1. Serrated flows and mechanical properties

Nanoindentation load-displacement (*P-h*) curves on each of the $Zr_{55}Cu_{30}Ni_5Al_{10}$ BMGs containing various H contents are given in Fig. 1. Note that the curves are displaced along the depth axis such that multiple curves could be accommodated on a single graph. A series of sudden displacement bursts or load drops can clearly be observed in the three curves; they are often described as “pop-ins” or serrated flows [34-39]. Furthermore, the number of pop-ins and their jump widths gradually decreased after hydrogenation (inset to Fig. 1).

These pop-in events were the initiation and expansion of one or more instantaneous shear bands. This phenomenon has been observed in many other BMG systems under nanoindentation [40]. Moreover, the nanohardness of the alloys and their elastic modulus generally decreased as the H content increased, indicating an H-induced softening effect (Fig. 2).

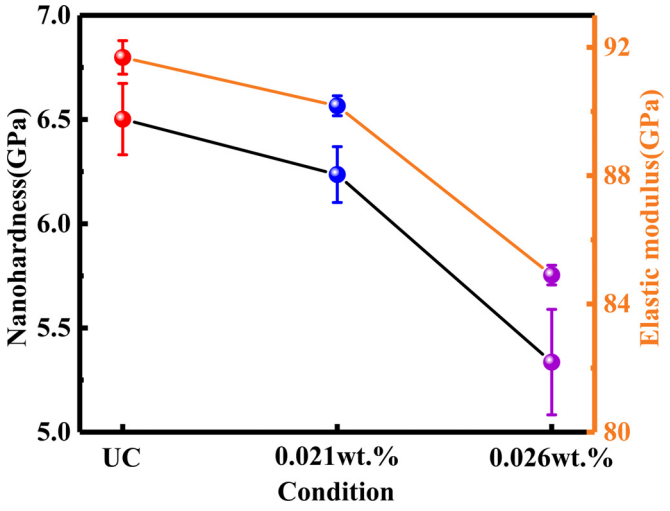

Fig. 2. Variation of the nanohardness and elastic modulus with the hydrogen content in the $Zr_{55}Cu_{30}Ni_5Al_{10}$ BMGs.

Further characterization of mechanical properties was performed using Vickers hardness tests. Representative SEM images of the $Zr_{55}Cu_{30}Ni_5Al_{10}$ BMGs with various H contents, and their measured Vickers hardness H_V are shown in Fig. 3. The Vickers hardness, H_V, is given in the unit of MPa, calculated by$0.102 \times F/A$, where F is the loading force, and A is the indentation surface area. These hardness data were basically consistent with the trend shown in Fig. 2, demonstrating that the observed trends were inherent to the materials rather than experimental contingencies. The SEM images indicated that the morphology around the indentation of the uncharged H alloy (UC) was relatively even, without obvious localized deformation. As the H content increased, the arc-shaped "ripple" lines around the indentation gradually densified, which corresponded to shear bands around the indented zone. Accordingly, it was reasoned that the addition of the trace H content serves to soften the $Zr_{55}Cu_{30}Ni_5Al_{10}$ BMGs, by increasing shear bands during deformation to enhance local plasticity. This finding is similar to what had been reported for some Zr-based BMGs [30, 41], but is contrary to the H-induced hardening phenomenon reported in other studies [42, 43]. Therefore, it was deemed to be appropriate to embark on an in-depth investigation of the interaction between hydrogen and the amorphous structures of the metallic glasses.

3.2. Nanoscale creep

Typical curves of creep depth versus holding time at selected penetration depths during nanoindentation showed that all curves exhibited two distinct phases, *i.e.*, Stage I and II (Fig. 4a). Stage I was instantaneous creep, which occurred approximately within the first 25 s of the load holding stage. Creep displacements increased rapidly during this stage, particularly at the beginning. Stage II occurred at 25–250 s of the load holding stage, and featured steady-state creep (i.e., the creep displacement gradually stabilized). Moreover, as the H content increased, the creep displacements increased. This feature was attributed to the H additions having a specific influence on the generation and movement of shear bands during creep of the MGs, which promoted local plastic deformation.

To further describe the creep behavior of MGs, the Kelvin model, which simulates deformation behavior in terms of a series of dashpots and linear springs, is commonly used [44–47]. Under the nanoindentation conditions, Yang et al. [48] have derived an elastic-viscoelastic-viscous (EVEV) model based on the generalized Kelvin model in order to describe indentation creep deformation. In this model, the stress-strain relationship is transformed into the relationship between load and displacement. As such, the total displacement, h, during the indentation creep is expressed as

$$h = h_e + \sum_{i=1}^{n} h_i\left(1 - e^{-t/\tau_i}\right) + t/\mu_0 \quad (1)$$

where h_e is the indentation depth at the first spring, h_i the indentation depth of the i^{th} Kelvin component, μ_0 the constant associated with the viscosity coefficient of the last dashpot, and τ_i the hysteresis time of the i^{th} component. In view of the much simpler relaxation process in BMGs [47], only two exponential terms in Eq. (1) need to be adopted for these materials. Accordingly, the typical displacement versus holding time curves can be successfully fitted with Eq. (1) with a correlation coefficient $R^2 > 0.99$ for all tests (Fig. 4b). The resulting fitting parameters are summarized in Table 1.

It is noted that as the H contents increases, h_1 ascends gradually while τ_1 and τ_2 show an increasing trend first followed by decrease. h_2, however, seems to unremarkably depend on the H contents. What is more, μ_0 increases as the H contents increases, implying a much more relaxed atomic packing for the hydrogenated MGs. This implication is in accordance with the lower hardness of the hydrogenated alloy, as indicated above.

The significance of the generalized Kelvin creep equation lies in its close relationship with other mechanical properties. The creep compliance, $J(t)$, is an important parameter that reflects mechanical properties, which can generally be obtained from the Kelvin creep equation [48, 49]:

$$J(t) = \frac{A_0}{P_0 h_{in}} h(t) = \frac{A_0}{P_0 h_{in}}\left[h_e + h_1\left(1 - e^{-t/\tau_1}\right) + h_2\left(1 - e^{-t/\tau_2}\right) + t/\mu_0\right] \quad (2)$$

where P_0 is the maximum load, A_0 is the contact area at the maximum load, and h_{in} is the maximum indentation depth. Based on the creep data and introduction of the related fitting parameters, Eq. (2) provides a means to calculate the creep compliance. The dependence of the creep compliance on the holding time for the $Zr_{55}Cu_{30}Ni_5Al_{10}$ BMGs with various hydrogen contents revealed a similar trend, *i.e.*, the initial creep compliance was constant but gradually increased with the holding time (Fig. 5a). This trend was essentially consistent with the variation of the creep compliance reported for La- [46], Ce- [47], Mg- [45] and Cu- [50]based BMGs. Wang et al. [51] have shown that under a constant load, the increased creep compliance is caused by the structural relaxation in BMGs. Additionally, Zhang et al. [52] have pointed out that the increased creep compliance in BMGs corresponds to a reduction in the elastic modulus ($E \sim 1/J(t)$). In this sense, Fig. 5a demonstrates that as the H content increased, the structure of the $Zr_{55}Cu_{30}Ni_5Al_{10}$ BMGs became relaxed, and the Young's modulus decreased. The finding is consistent with the E values shown in Fig. 2.

The retardation spectra ($L(\tau)$) of the $Zr_{55}Cu_{30}Ni_5Al_{10}$ BMGs was estimated from the following approximate expression [53]:

$$L(\tau) = \left[\left(1 + \frac{t}{\tau_1}\right)\frac{h_1}{\tau_1}e^{-t/\tau_1} + \left(1 + \frac{t}{\tau_2}\right)\frac{h_2}{\tau_2}e^{-t/\tau_2}\right]\frac{A_0}{P_0 h_{in}}t|_{t=2\tau} \quad (3)$$

The results as a function of the H content in the BMGs established that the retardation spectra of the samples with different hydrogen contents were composed of two relatively-independent retardation peaks - one narrow and the other wide (Fig. 5b). The two peaks were similar to the fast β and slow α relaxations in BMGs, indicating that the two relaxation states were present in the current BMGs. Ocelik et al. [54] have also reported this phenomenon in the study of amorphous ribbons, suggesting that it is

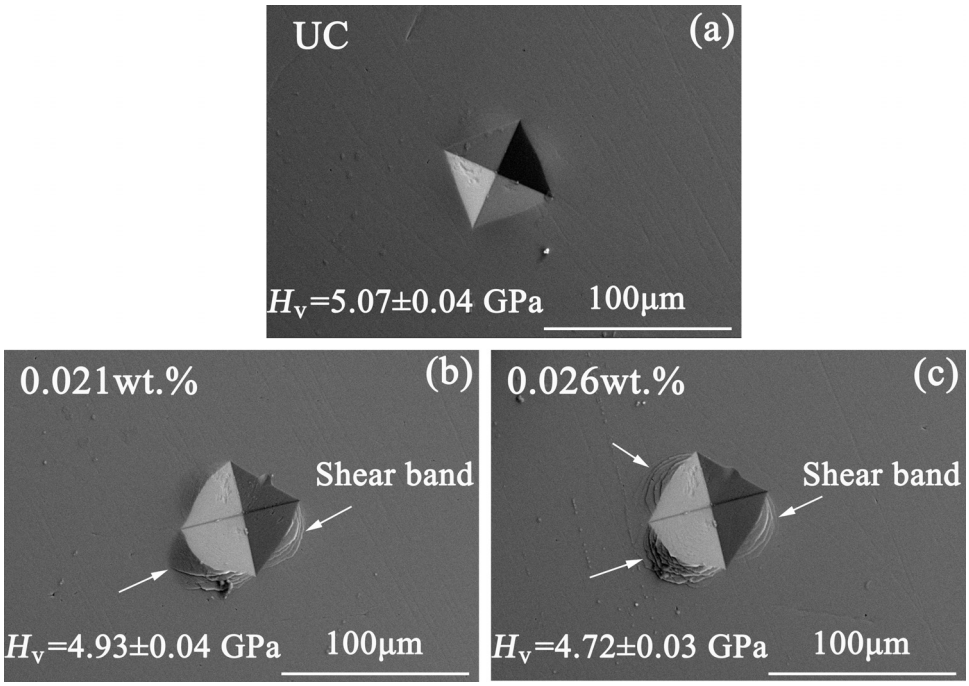

Fig. 3. Representative SEM images of the Vickers hardness impressions of the $Zr_{55}Cu_{30}Ni_5Al_{10}$ BMGs with various H contents.

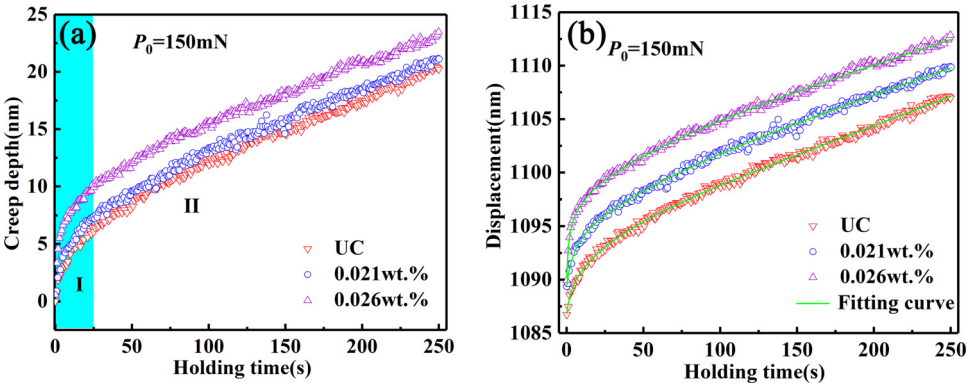

Fig. 4. Typical displacement versus holding time curves for the $Zr_{55}Cu_{30}Ni_5Al_{10}$ BMGs with various H contents, showing (a) the division of the two-stage creep, and (b) the fitting of the curves using the elastic-viscoelastic-viscous (EVEV) model.

Table 1
Fitting parameters of the nanoindentation-creep curves of the $Zr_{55}Cu_{30}Al_{10}Ni_5$ BMGs with various H contents using Eq. (1).

Alloy	H content C_H(wt.%)	h_e(nm)	h_1(nm)	τ_1(s)	h_2(nm)	τ_2(s)	μ_0(s/nm)	R^2
$Zr_{55}Cu_{30}Al_{10}Ni_5$	0	1086.7	2.34	3.08	4.37	28.12	18.27	0.99737
	0.021	1089.3	3.77	4.74	4.18	50.57	19.97	0.99621
	0.026	1089.9	5.79	2.15	4.61	37.69	20.56	0.99705

related to chemical and topological short range ordering in the relaxation process. Castellero et al. [45] have pointed out that the width and intensity of the peak are related to the size of the defect (soft region), respectively. Small defects exist in open volume areas, similar to a Bernal gap, while large holes are thermally instable. This trend means that each peak represents a different material-transport mechanism or distinct type of flow defects in amorphous structures. Notably, as the hydrogen content increases, the first peak exhibits the increased intensity, and the relaxation time initially increases and then decreases (Fig. 5b). In simple terms, these results indicate that the effect of hydrogen additions is to make the structure of the BMGs more relaxed. As a result, the aggregate of the corresponding defects increased, and the activation of the remaining defects became easier. However, the influence of hydrogen content on the second peak's intensity and position is far less clear.

4. Discussion

The experimental results described in this study clearly indicate that the deformation behavior and mechanical properties of the $Zr_{55}Cu_{30}Ni_5Al_{10}$ BMGs are closely related to their H contents. This trend was caused by the presence of H, which resulted in material softening and relaxation of the internal structure. To provide clarity as to why such mechanical and structural responses occurred

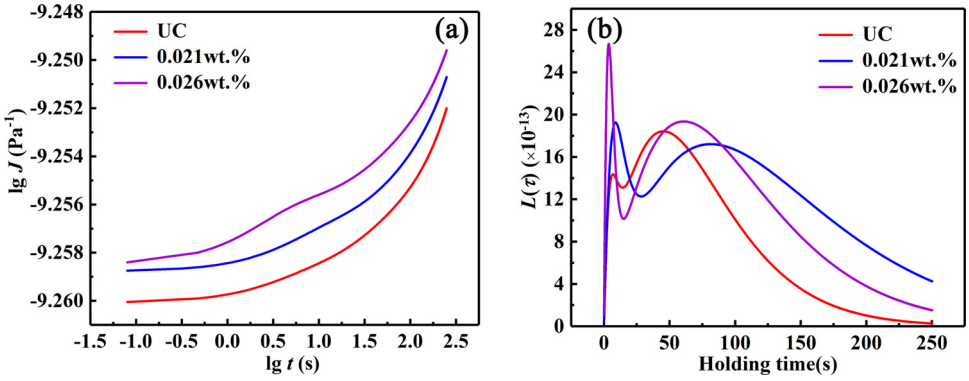

Fig. 5. (a) Creep compliance spectra and (b) retardation spectra of the $Zr_{55}Cu_{30}Ni_5Al_{10}$ BMGs with various H contents.

as the H content was raised, we investigate now how H can affect the internal flow units of these glassy materials.

4.1. Evolution of internal flow units during the loading stage

The lack of linear and planar defects in amorphous structures, such as dislocations and grain boundaries, makes BMGs only plastically deform by the motion of internal flow units [55-57]. When BMGs are influenced by external forces, internal flow units are formed by relative sliding between unstable atomic clusters and residual free volumes. With the accumulation of STZs, a blocking state can form and, as the shear action strengthens with increasing stress, this blocking state can lose stability such that an incipient shear zone can form and expand. This process causes intermittent shear collapse, corresponding to the serration-flow phenomenon on nanoindentation curves [58, 59]. Therefore, each serration flow phenomenon represents the formation and expansion of one or more shear bands [40]. This feature also implies that if the serration flow is associated with internal flow units, then it is plausible that the deformation behavior of MGs can be explained.

Recent serration-flow studies have shown that the serration process comprises repeated cycles of sudden stress drops prior to being generally followed by an elastic-loading portion [58]. A serration flow is interpreted to represent a full cycle of the shear-band movement, including nucleation, propagation, and arrest. Shear-band propagation, seen as stress drops, corresponds to a stage of extended, uniform flows within the band under a transient stress. This trend results in discontinuous serration steps on nanoindentation curves, of a magnitude depending on the stress relaxation and system characteristics [60]. Therefore, it is reasonable to regard the intersection of the two serration-flow stages on the nanoindentation-loading curve as a transition from the instantaneous elastic strain to plastic deformation. This feature is similar to the first pop-in observed during the loading stage of the spherical indentations [61]. The difference here is that the first pop-in corresponds to a sparse shear band (perhaps only one main shear band) being suppressed under a high shear stress, while other serration flows in the nanoindentation-loading curve correspond to multiple shear bands being activated under a relatively-low shear stress. This trend implies that statistical analysis of the shear stress at the onset of this serration flow during the loading stage can permit a connection to the CSM model. Moreover, it may elucidate the salient structural changes in the material at this point.

Prior to statistical analysis of the shear stress, effective serrations first need to be isolated and identified, because background noise in the experimental equipment could also be the cause of several higher frequency and lower amplitude serrations on the nanoindentation curve. The accuracy of statistical analysis can be affected by the large amount of noise serrations. Therefore noise-reduction procedures must be used to avoid statistical errors [62]. In previous studies, the noise was removed, using a polynomial function based on the serration size of the nanoindentation-holding stage [63-66]. However, this method suffers from a serration size error, Δh_{err} [67], in each serration, and the accumulated experimental error could be fairly large. Hence, an exponential function was used to describe the variation of the displacement rate with time (dh/dt-t), where dh/dt was regarded as the serration size. The exponential function [67]was given as:

$$\frac{dh}{dt} = C \cdot \left[\exp\left(A \cdot t^B\right) - 1\right] + D \tag{4}$$

where A, B, C, and D are the fitting parameters. Eq. (4) was fitted to the dh/dt-t data in the loading stage to obtain a baseline (Fig. 6a; correlation coefficient, $R^2 > 0.99$, for all tests). After the baseline subtraction, the processed data were linearly fitted again using [67]:

$$\frac{dh}{dt} = K \cdot t + M \tag{5}$$

where M is the fitting parameters. The above step were repeated until the slope of Eq. (5), K, was close to 0, which effectively eliminated the influence of external noise and increased indentation depth such that the processed serration events were clearly visible as a function of the load time, t (Fig. 6b). As the first pop-in phenomenon for these $Zr_{55}Cu_{30}Ni_5Al_{10}$ BMGs generally occurred at ~330 nm (~20 s), it is reasonable to infer that the majority of the irregular serrations occurred after ~20 s. Thus, the abscissa in Fig. 6b was started at t = 20 s. Moreover, it was observed that the serrations were more intense at the beginning of the indentation and then become relatively stable. This trend was noted because at the initial stages of plastic deformation, *i.e.*, at the bending portion of the dh/dt-t curve, serrations mainly arose from the formation of highly-discrete, localized shear bands [58], with the serration sizes progressively decreased due to the formation and expansion of a larger number of shear bands.

Subsequently, the shear stress of an MG was obtained from these effective serrations, and can be expressed by [9]

$$\tau = \frac{H}{3 \times \sqrt{3}} \tag{6}$$

where H is the hardness, calculated by mean pressure [68-70]:

$$H = \frac{P}{A(h_c)} \tag{7}$$

where A is the contact area at an applied indentation load of P, the area function, $A(h_c)$, for a perfect Berkovich indenter can be written as [68-70]:

$$A(h_c) = 24.56h_c^2, \tag{8}$$

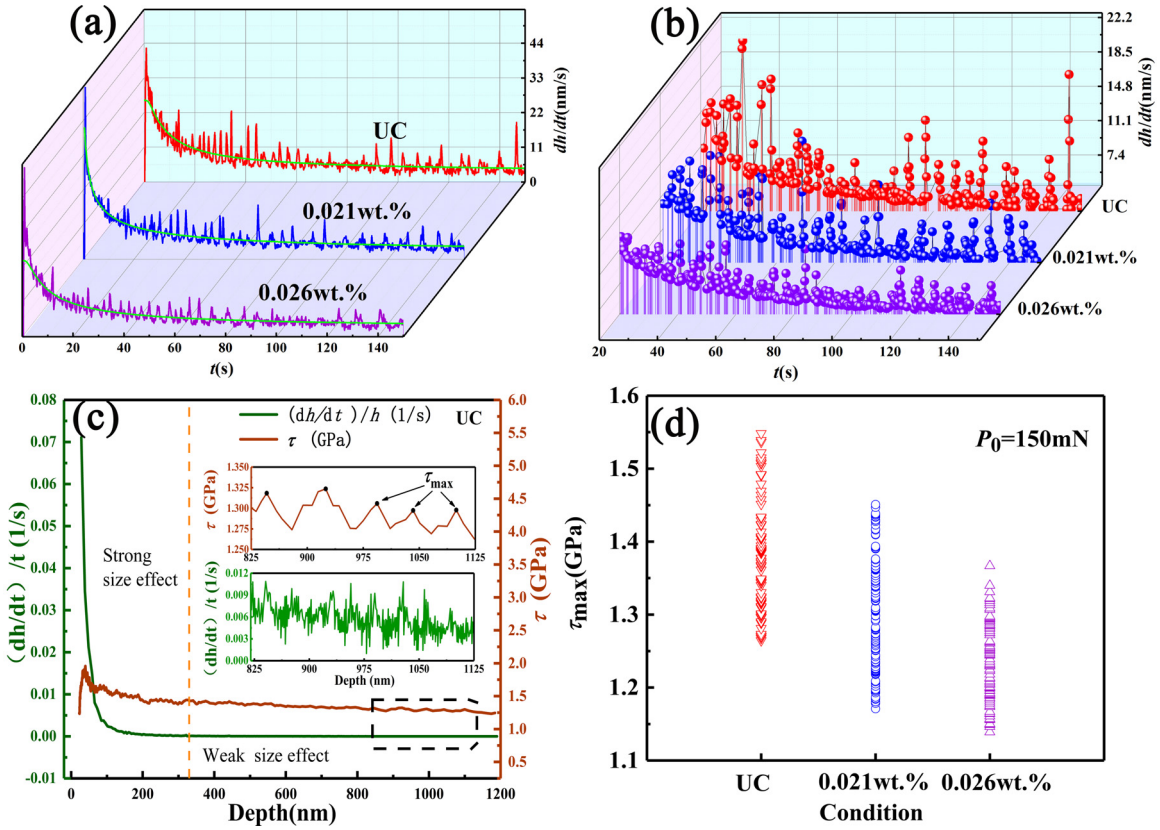

Fig. 6. (a) Raw data and fitting curve (cyan solid line) for the change in penetration depth with time as a function of time throughout the loading process, dh/dt vs. t, in uncharged and charged alloys. (b) Corresponding extracted serration bursts versus time after 20 s of loading in uncharged and charged alloys. (c) Taking uncharged samples as an example, indentation-size effect can be observed on curves of shear stress, τ, vs. penetration depth, h, (brown line) and indentation strain rate, $\dot{\varepsilon}$, vs. penetration depth, h, (dark green line). The inset is the partial enlarged view. (d) Variation in the maximum shear stress identified by the intersection of the two stages in each serration event in uncharged and charged alloys.

where $h_c = h - \varepsilon \times P/S$ is the contact depth at an indentation load of P, S is the contact stiffness quantified using the DNT method of nanoindentation, and $\varepsilon = 0.75$ is a constant. Substituting Eqs. (7) and (8) into Eq. (6) can obtain:

$$\tau = \frac{P}{24.56 \times 3 \times \sqrt{3} \cdot (h - \varepsilon \cdot P/S)^2} \tag{9}$$

The shear stress (τ) and the indentation strain rate ($\dot{\varepsilon} = \frac{1}{h} \times \frac{dh}{dt}$) as a function of the displacement into the surface is shown in Fig. 6c. The indentation-size effect (ISE) is manifested as an increase in hardness (or shear stress,$\tau = 3\sqrt{3} \times H$) with decreasing the impression size [71], and this phenomenon can be clearly observed at the initial stage for indentation depths up to ~330 nm (we refer to this feature as a "strong size effect" stage). However, once the penetration depth exceeds this value, the shear stress oscillates over a narrow range (which we term as the "weak size effect" stage). In other words, as the indentation deepens, the indentation-size effect gradually weakens. This phenomenon suggests that the ISE is minimal in the weak size effect stage. Moreover, the maximum shear stress, τ_{max}, is the shear stress at the transition from elasticity to plasticity and thus, could be readily identified by the beginning of each serration event. The τ_{max} values vary in a narrow range with increasing indentation depth for each $Zr_{55}Cu_{30}Ni_5Al_{10}$ BMG (inset in Figs. 6c and 6d). In addition, the effect of hydrogen here is clearly apparent by the decrease in τ_{max} with increasing the hydrogen concentration C_H (Fig. 6d).

Accordingly, the cumulative distributions of τ_{max} in these BMGs were plotted (Fig. 7a). Based on Schuh's work [72], both the thermally-assisted and stress-biased processes can affect the yield strength and cause it to fluctuate within a certain range. This is because the thermal noise sometimes favors yielding but works against it at other times. Hence, the cumulative distribution function, f, of serration events can be described as a function of τ_{max} beneath the indenter in terms of:

$$f = 1 - \exp\left[-\frac{kT\gamma}{V^*(d\tau/dt)} \exp\left(-\frac{\Delta F^*}{kT}\right) \exp\left(\frac{\tau V^*}{kT}\right)\right], \tag{10}$$

where k is the Boltzmann constant, T is the experimental temperature, γ is the attempt frequency, ΔF^* is the Helmholtz activation energy, and V^* is the activation volume of the serrations. In general, V^* can be calculated from the slope of the linear relationship between $\ln[\ln(1\text{-}f)^{-1}]$ vs. τ_{max} by converting Eq. (10) into:

$$\ln\left[\ln(1-f)^{-1}\right] = \left\{\frac{\Delta F^*}{kT} + \ln\left[\frac{kT}{V^*(d\tau/dt)}\right]\right\} + \frac{\tau V^*}{kT} \tag{11}$$

The correlations between $\ln[\ln(1\text{-}f)^{-1}]$ and τ_{max} for the three BMGs show that a linear relationship clearly did not exist in the full range of experiments, which is similar to results reported in previous studies (Fig. 7b) [73]. Considering that the elastic-plastic transition deformation process of the tested BMGs was a thermally-activated process, the activation volume should be related to the local shear stress, which might be responsible for this nonlinear relationship. To account for the observed nonlinearity, Eq. (11) was modified by introducing a quadratic polynomial [73]:

$$V^*(\tau) = V_0 + V_1\tau + V_2\tau^2 \tag{12}$$

where V_0, V_1, and V_2 are fitting parameters. The modified equation best describes the experimental data with a fitting correlation co-

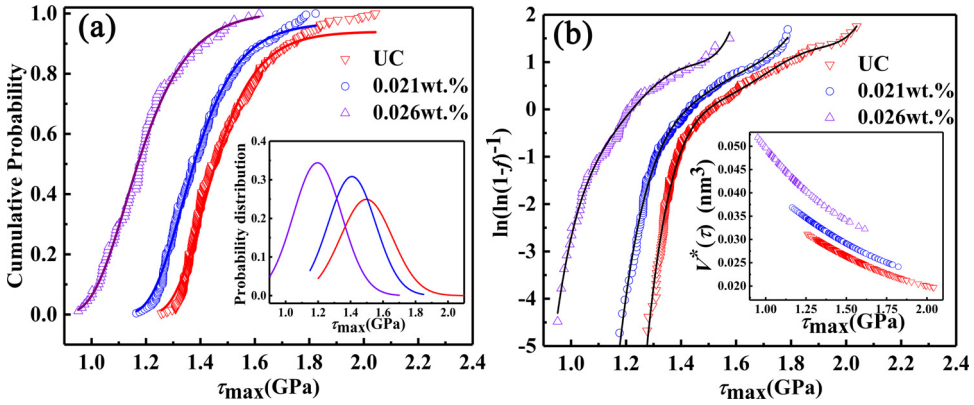

Fig. 7. (a) Cumulative probability distributions of τ_{max} at serrations in uncharged and charged alloys; inset shows the probability distributions of corresponding, τ_{max}. (b) The correlation between $\ln[\ln(1\text{-}f)^{-1}]$ and τ_{max} for these uncharged and charged alloys; introducing Eq. (12) produced a good agreement with the data (solid black lines), and the inset shows the range of V^* values for the uncharged and charged alloys.

Table 2
Correlation parameters for the internal flow units in the loading stage using the serration-flow statistic method.

Alloy	H content C_H (wt.%)	Activation Volume V^* (nm^3)	STZ volume Ω (nm^3)	STZ size (atom)	STZ activation energy W(kJ/mol)
$Zr_{55}Cu_{30}Al_{10}Ni_5$	UC	0.02824±0.0007	0.6162±0.021	41±2	36.8 ± 1.4
	0.021	0.03183±0.0011	0.6949±0.024	46±2	40.8 ± 1.6
	0.026	0.04304±0.0016	0.9400±0.036	62±3	61.4 ± 2.4

efficient as high as 0.99 (Fig. 7b). Using the fitting parameters, V_0, V_1, and V_2, the activation volume ranges of the BMGs with various hydrogen contents were obtained and plotted. This feature indicated that the activation volume, V^*, was significantly improved after hydrogenation, with V^* values in the range of 0.02 - 0.05 nm^3 (Inset of Fig. 7).

From the activation volumes determined above, the most fundamental internal flow unit size for plastic flows in the BMGs was estimated using the CSM of Johnson and Samwer [22], given as:

$$\Omega = \frac{\tau_0}{6R_0 G\gamma_c^2 \xi (1-\tau/\tau_0)^{1/2}} V^*, \tag{13}$$

where Ω is the STZ volume, G is the shear modulus, R_0 is a constant ≈ ¼, and ξ is the correction coefficient for matrix binding around internal flow units, which is equal to 3, γ_c is the critical shear strain ($\gamma_c = \tau/G$), and τ and τ_0 are, respectively, the critical shear strengths at the experimental temperature and 0 K.

For the activation of a flow unit, these stresses have to exceed a potential energy barrier, W, which can be expressed by the equation [74]

$$W = \left(8/\pi^2\right)\gamma_c^2 \xi G \Omega \tag{14}$$

According to the densely-packed hard-spheres model for BMGs [75], the number of atoms contained in the flow unit can be calculated approximately using the average atomic radius,$r \approx (\sum_i^n A_i r_i^3)^{\frac{1}{3}}$, where A_i and r_i are, respectively, the atomic fraction and radius of each element, respectively. Based on the glass-transition temperature T_g, the shear modulus, G, and other parameters for these BMGs, the computed results demonstrated that when the H content increased to 0.026 wt.%, the internal flow unit volume, size, activation energy, and other results from these BMGs significantly increased (by ~52.4%, Table 2). Intuitively, a change in the internal flow units can explain the weakness of the pop-in phenomenon, which means that the number of pop-ins and their jump widths gradually decreased after hydrogenation (inset to Fig. 1) and the increased number of shear bands around the Vickers hardness indentations (inset to Fig. 2). The addition of hydrogen enables the BMGs to generate internal flow units with a larger volume and size for the process of plastic deformation. The large-sized internal flow units induced significant local strain fields and excessive free volumes, which in turn facilitate the activation of secondary as well as tertiary flow units in the region of the first flow unit [21, 76]. The high-density of potential flow units activated can reach the percolation limit, thereby promoting the gestation and proliferation of denser shear bands [14]. In contrast, an increased flow unit size implies an increased number of loose atomic clusters and free volumes in the material [61], which also make the mechanical properties, especially strength and plasticity, vary significantly. Hence, the macroscopic plastic behavior of the Zr-based BMGs can be closely tied to the internal flow units.

4.2. Evolution of internal flow units during creep

From the standpoint of the microscopic mechanism of plastic deformation in BMGs, creep behavior during the load-bearing phase is also achieved by the activation of internal flow units and cooperative shearing. Pan et al. [26] have characterized flow units in BMGs by measuring the strain-rate sensitivity of hardness using a rate-jump method based on the Johnson-Sawmer CSM model. Here, the volume of the STZ Ω was expressed as:

$$\Omega = \frac{\mathrm{kT}}{C' m H} \tag{15}$$

where k is the Boltzmann constant, T the experimental (absolute) temperature, H the indentation hardness, $C' = \frac{2R_0\xi}{\sqrt{3}} \cdot \frac{G\gamma_C^2}{\tau_0}(1-\frac{\tau}{\tau_0})^{1/2}$ a constant related to T_g and computed according to the Johnson and Samwer's theory [22], and m the strain-rate sensitivity during the period of creep deformation. The most critical aspect of the above parameters was the determination of the strain-rate sensitivity, which was estimated from the slope of the double-log plot of the hardness, H, vs. strain rate, $\dot{\varepsilon}$ [77, 78], *i.e.*,

$$m_{\mathrm{creep}} = \frac{\partial \ln H}{\partial \ln \dot{\varepsilon}} \tag{16}$$

For the nanoindentation-creep process, the strain rate, $\dot{\varepsilon}$, was expressed as [26]:

$$\dot{\varepsilon} = \frac{1}{h} \cdot \frac{dh}{dt} \tag{17}$$

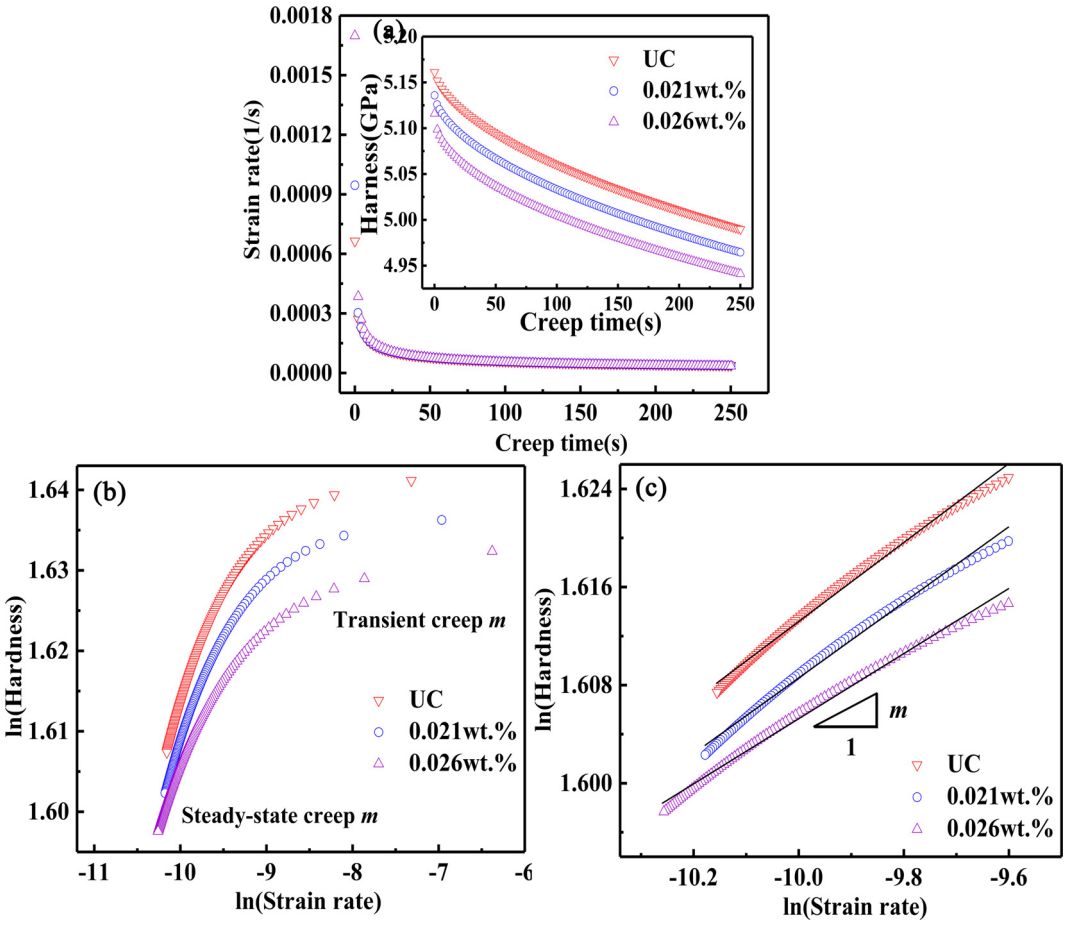

Fig. 8. (a) Change in the stress and strain rate vs. creep time for the uncharged and charged BMGs. (b) Log-log correlation between the indentation stress and strain rate during creep for these uncharged and charged alloys. (c) The strain-rate sensitivity, *m*, estimated by linear fitting of the steady-state portion of the creep curves.

Table 3
Correlation parameters of internal flow units in the holding stage determined by the creep method.

Alloy	H content C_H (wt.%)	Strain rate sensitivity *m*	STZ volume Ω (nm^3)	STZ size (atom)	STZ activation energy *W*(kJ/mol)
$Zr_{55}Cu_{30}Al_{10}Ni_5$	UC	0.0322±0.003	2.278±0.026	165±2	135.6 ± 1.6
	0.021	0.0308±0.002	2.473±0.012	180±1	145.2 ± 0.7
	0.026	0.0265±0.004	3.362±0.023	245±1	183.7 ± 1,3

where *h* is the instantaneous indentation depth during nanoindentation creep, *t* the corresponding time, and *dh*/*dt* the creep displacement rate, which was fitted and differentiated using the empirical formula, $h(t) = h_0 + a(t\text{-}t_0)^b + kt$, where h_0 and t_0 are the displacement and time at the beginning of creep, respectively, and *a, b*, and *k* fitting parameters.

For a Berkovich indenter, the hardness, *H*, during indentation creep also can be obtained by Eqs. (7) and (8) [79]:

$$H = \frac{P}{24.56 \times (h - \varepsilon \times P/S)^2}. \quad (18)$$

Using such relationships, the hardness and strain rate vs. creep time of the BMGs with various H contents was evaluated. Results are shown in Fig. 8a and indicate that the strain-rate curves of the three BMGs almost coincide, but with the indentation stress significantly reduced after the alloys were charged with hydrogen. The correlation between the hardness and strain rate during creep was used to deduce the strain-rate sensitivity (Fig. 8b), using the slope of the linear-regression lines for the steady-state creep region (Fig. 8c).

The results of creep tests showed that the influence of hydrogen was also evident during the holding stage (Table 3). Indeed, an increase in the volume, size, and activation energy of the internal flow units with increasing the H content was clearly observed, which is in a qualitative agreement with the results of the serration-flow statistics method. Therefore, the calculated changes in the internal flow units are consistent with the more pronounced creep deformation in BMGs, where the easy activation of a larger-sized flow unit promotes the formation, proliferation, and movement of shear bands, together with the enhanced creep flow and structural relaxation. Furthermore, it was also found that the size, volume, and related parameters of the internal flow units estimated by the creep method were slightly higher than those evaluated by the serration-flow statistics method. The appearance of this phenomenon was possibly due to the following two reasons: (i) although both methods represent quasi-static deformation, the equivalent strain rate during the loading stage of nanoindentation was at least two orders of magnitude larger than the creep strain rate; (ii) the testing conditions and deformation kinetics were quite different. In the serration flow statistic method, with increasing the indentation depth, a larger deformed volume is involved, and thus, a larger number of STZs would be active cooperatively, leading to a decrease in the strength or hardness. However, in the creep

method, a constant load was applied during the holding stage, which made the creep flows of the material more homogeneous and slower [80].

4.3. Influence of hydrogen on the deformation behavior and mechanical properties of BMGs

Hydrogen is an active gas. However, H atoms are the smallest of all elements and hence, are similar to the free volume size. It is therefore reasonable to expect that H–H and H-free volume interactions in BMGs play a vital role in determining the deformation behavior and mechanical properties of H-charged BMGs. Hydrogen in BMGs can be partitioned into the mobile (weakly-bound) and immobile (strongly-bound or trapped) parts. While the mobile H naturally and readily diffuses, immobile H belongs to a trapped state [28]. At present, three possible mechanisms for mobile H-assisted softening have been proposed, based on the "spacer" concept [27]. Specifically, after H enters a BMG, mobile H acts mostly as a simple "spacer" at interstitial sites, expanding the interatomic spacing without interactions (or strong binding) with the surrounding metallic atoms. The mobile "spacers" always around the liquid-like regions act as the catalyst for the formation of STZ in the H-charged BGMs[81]. Under stress, it is easy to produce such "superabundant vacancies," making movement more intense between atoms. Conversely, the immobile H may have a dominant role in hindering plastic deformation, *i.e.*, these hydrogen atoms induce hardening in highly-immobile H alloys. The strong combination of immobile H with surrounding metallic atoms results in the formation of a densely-arranged structure with a specific chemical and geometric configuration, which is similar to the short-range ordering of hydrides. In this case, the dense packing restricts local atomic movement. Hence, it becomes difficult to induce deformation by restricting atoms to participate in the activation of internal flow units [27, 28].

From an electronic perspective, trace doping with H has been seen to cause a downward shift in the binding energy for each element [6, 9, 81, 82]. The core-level binding energy is closely related to the characteristics of the local chemistry and the configurational environment of the constituent atoms [83]. The observed decrease in binding energy indicates that the local metallic bonding around H atoms has become "softened," from which it can be concluded that H additions results in the valence electron transfer from the Zr-3*d* band to the Zr-H bonding state, which then serves to weaken the neighboring metallic bonds. Using Troiano's hydrogen-enhanced decohesion theory as a basis [84, 85], it is plausible that H-1 *s* electrons transfer to the Zr-3*d* conduction band and thus, act to enhance repulsive forces between the metallic ions, which would also weaken the Zr-Cu and Zr-Al pair binding energies near these H atoms. Therefore, H additions can be expected to induce more easily-activated "soft spots" in glassy systems, thus promoting the formation and aggregation of STZs. These observations also explain why H additions can significantly reduce the elastic modulus and hardness of BMGs, again based on the metal decohesion theory [86]. Moreover, the weakening of metal-metal bonds in the easily deformable zones means that it becomes easier to eliminate the fixed position and move to a nearby site.

With regards to the internal flow units, after the hydrogenation of the $Zr_{55}Cu_{30}Ni_5Al_{10}$ BMGs, flow unit dimensions (STZ volume) increase in response to the external stimulus (stress). When the applied stress exceeds the yield stress, flow units are able to overcome the energy barrier and hence, become irreversible [14]. In addition, the yield stress can be significantly reduced after hydrogenation, rendering more flow units irreversible. Once a flow unit is activated, its environment can be considered as prior activation sites for secondary and subsequent flow units, thereby easily aggregating such flow units and inducing cooperative flows to generate shear bands. The formation, proliferation, crossing, and hindrance of shear bands can promote the dilatation of the BMG structure to improve local plasticity, such that mechanical softening and local deformation are more likely to occur.

5. Conclusions

Based upon the above experimental observations and theoretical analysis of the role of hydrogenation in altering the internal flow units in Zr-based bulk-metallic glasses during nanoindentation, the following conclusions can be made:

1 The serrated flow, hardness, elastic modulus, and local plasticity were all found to strongly depend on the hydrogen content in $Zr_{55}Cu_{30}Ni_5Al_{10}$ BMGs. With increasing the H content, the pop-in phenomenon during nanoindentation gradually decreased. The hardness and elastic modulus were significantly reduced as the local plasticity effectively improved, indicating an H-induced softening effect.
2 The creep properties of the $Zr_{55}Cu_{30}Ni_5Al_{10}$ BMGs during the nanoindentation-holding stage exhibited a very strong correlation with the H content. As the H content increased, the creep became increasingly severe. The compliance index and retardation spectrum also increased, revealing H-induced structural relaxation.
3 Based on the cooperative shear model theory, the serration-flow statistics and creep method were used to determine the influence of hydrogen on the volume, size, and activation energy of the internal flow units during nanoindentation loading and holding stages. Results suggested that the increased H content made the internal flow units expand, such that the interior of the materials became relaxed, yielding shear-band proliferation, and thus enhanced plasticity. In turn, the aggregation of these internal flow units reduced the critical stress required for shear-band-mediated plastic deformation, thereby causingstructural relaxation and mechanical softening.

Acknowledgments

The present work was supported the National Natural Science Foundation of China (51401129), Natural Science Foundation of Liaoning Province (2019-ZD-0216, 20180510056), Foundation of Liaoning Province Education Administration (LQGD2019001). PKL thanks the support from the National Science Foundation (DMR-1611180 and 1809640) with the program directors, Drs. J. Yang, G. Shiflet, and D. Farkas. ROR was supported by the U.S. Department of Energy, Office of Science, Office of Basic Energy Sciences, Materials Sciences and Engineering Division under Contract No. DE-AC02–05-CH11231.

References

[1] H.J. Lin, M. He, S.P. Pan, L. Gu, H.W. Li, H. Wang, L.Z. Ouyang, J.W. Liu, T.P. Ge, D.P. Wang, W.H. Wang, E. Akiba, M. Zhu, Acta Mater. 120 (2016) 68–74.
[2] S.-i. Yamaura, M. Sakurai, M. Hasegawa, K. Wakoh, Y. Shimpo, M. Nishida, H. Kimura, E. Matsubara, A. Inoue, Acta Mater. 53 (13) (2005) 3703–3711.
[3] M.D. Dolan, N.C. Dave, A.Y. Ilyushechkin, L.D. Morpeth, K.G. McLennan, J. Memb. Sci. 285 (1) (2006) 30–55.
[4] F. Dong, M. He, Y. Zhang, L. Luo, Y. Su, B. Wang, H. Huang, Q. Xiang, X. Yuan, X. Zuo, B. Han, Y. Xu, J. Non Cryst. Solids 481 (2018) 170–175.
[5] R. Kirchheim, F. Sommer, G. Schluckebier, Acta Metallurgica 30 (6) (1982) 1059–1068.
[6] F. Dong, M. He, Y. Zhang, L. Luo, Y. Su, B. Wang, H. Huang, Q. Xiang, X. Yuan, X. Zuo, B. Han, Y. Xu, Int. J. Hydrogen Energy 42 (40) (2017) 25436–25445.
[7] D. Granata, E. Fischer, J.F. Löffler, Acta Mater. 99 (2015) 415–421.
[8] N. Eliaz, D. Eliezer, Adv. Perform. Mater. 6 (1) (1999) 5–31.
[9] F. Dong, M. He, Y. Zhang, B. Wang, L. Luo, Y. Su, H. Yang, X. Yuan, Mater. Sci. Eng. 759 (2019) 105–111.
[10] K.W. Park, Y. Shibutani, Int. J. Hydrogen Energy 36 (15) (2011) 9324–9334.
[11] S. Jayalakshmi, K.B. Kim, E. Fleury, J. Alloys Compd. 417 (1) (2006) 195–202.
[12] F.Y. Dong, Y.Q. Su, L.S. Luo, L. Wang, S.J. Wang, L.J. Guo, H.Z. Fu, Int. J. Hydrogen Energy 37 (19) (2012) 14697–14701.

[13] D. Suh, R.H. Dauskardt, Scr. Mater. 42 (3) (2000) 233–240.
[14] S.T. Liu, Z. Wang, H.L. Peng, H.B. Yu, W.H. Wang, Scr. Mater. 67 (1) (2012) 9–12.
[15] W.H. Wang, Y. Yang, T.G. Nieh, C.T. Liu, Intermetallics 67 (2015) 81–86.
[16] J.C. Qiao, Q. Wang, J.M. Pelletier, H. Kato, R. Casalini, D. Crespo, E. Pineda, Y. Yao, Y. Yang, Prog. Mater. Sci. 104 (2019) 250–329.
[17] W. Li, H. Bei, Y. Tong, W. Dmowski, Y.F. Gao, Structural heterogeneity induced plasticity in bulk metallic glasses: from well-relaxed fragile glass to metal-like behavior, 103(17) (2013) 171910.
[18] W. Li, Y. Gao, H. Bei, Sci. Rep. 5 (1) (2015) 14786.
[19] Z. Wang, P. Wen, L.S. Huo, H.Y. Bai, W.H. Wang, Appl. Phys. Lett. 101 (12) (2012).
[20] F. Spaepen, Acta Metallurgica 25 (4) (1977) 407–415.
[21] A.S. Argon, Acta Metallurgica 27 (1) (1979) 47–58.
[22] W.L. Johnson, K. Samwer, Phys. Rev. Lett. 95 (19) (2005) 195501.
[23] C. Bennemann, C. Donati, J. Baschnagel, S.C. Glotzer, Nature 399 (6733) (1999) 246–249.
[24] A. Furukawa, H. Tanaka, Nat. Mater. 8 (7) (2009) 601–609.
[25] M. Zink, K. Samwer, W.L. Johnson, S.G. Mayr, Phys. Rev. B 73 (17) (2006).
[26] D. Pan, A. Inoue, T. Sakurai, M.W. Chen, Proc Natl. Acad. Sci. 105 (39) (2008) 14769.
[27] Y. Zhao, I.-.C. Choi, M.-.Y. Seok, U. Ramamurty, J.-.Y. Suh, J.-ii. Jang, Scr. Mater. 93 (2014) 56–59.
[28] Y.K. Zhao, I.C. Choi, M.Y. Seok, M.H. Kim, D.H. Kim, U. Ramamurty, J.Y. Suh, J.I. Jang, Acta Mater. 78 (2014) 213–221.
[29] F. Dong, S. Lu, Y. Zhang, L. Luo, Y. Su, B. Wang, H. Huang, Q. Xiang, X. Yuan, X. Zuo, J. Alloys Compd. 695 (2017) 3183–3190.
[30] W. Dandana, M.A. Yousfi, K. Hajlaoui, F. Gamaoun, A.R. Yavari, J. Non Cryst. Solids 456 (2017) 138–142.
[31] G.M. Pharr, J.H. Strader, W.C. Oliver, J. Mater. Res. 24 (3) (2009) 653–666.
[32] G.Y. Zhou, J. Guo, J.Y. Zhao, Q. Tang, Z.N. Hu, Metals-Basel 10 (1) (2020).
[33] J.Y. Sun, W. Wu, M.Z. Ling, B. Bhushan, J. Tong, RSC Adv. 6 (82) (2016) 79106–79113.
[34] L. Liu, K.C. Chan, Mater. Lett. 59 (24–25) (2005) 3090–3094.
[35] Y. Zhang, J.P. Liu, S.Y. Chen, X. Xie, P.K. Liaw, K.A. Dahmen, J.W. Qiao, Y.L. Wang, Prog. Mater. Sci. 90 (2017) 358–460.
[36] W.H. Jiang, F. Jiang, F.X. Liu, Y.D. Wang, H.M. Dang, F.Q. Yang, H. Choo, P.K. Liaw, Mater. Sci. Tech.-Lond. 28 (2) (2012) 249–255.
[37] L.P. Yu, S.Y. Chen, J.L. Ren, Y. Ren, F.Q. Yang, K.A. Dahmen, P.K. Liaw, J. Iron. Steel Res. Int. 24 (4) (2017) 390–396.
[38] R. Sarmah, G. Ananthakrishna, B.A. Sun, W.H. Wang, Acta Mater. 59 (11) (2011) 4482–4493.
[39] L. Cheng, Z.M. Jiao, S.G. Ma, J.W. Qiao, Z.H. Wang, J. Appl. Phys. 115 (8) (2014).
[40] B.A. Sun, H.B. Yu, W. Jiao, H.Y. Bai, D.Q. Zhao, W.H. Wang, Phys. Rev. Lett. 105 (3) (2010) 035501.
[41] Q.J. Zhou, J.Y. He, X.P. Hao, W.Y. Chu, L.J. Qiao, Mat. Sci. Eng. a-Struct. 437 (2) (2006) 356–359.
[42] S. Jayalakshmi, E. Fleury, D.J. Sordelet, J. Phys. 144 (2009).
[43] G.B. Shan, J.X. Li, Y.Z. Yang, L.J. Qiao, W.Y. Chu, Mater. Lett. 61 (8–9) (2007) 1625–1628.
[44] D. Chiang, J.C.M. Li, Polymer (Guildf) 35 (19) (1994) 4103–4109.
[45] A. Castellero, B. Moser, D.I. Uhlenhaut, F.H.D. Torre, J.F. Löffler, Acta Mater. 56 (15) (2008) 3777–3785.
[46] W.H. Li, K. Shin, C.G. Lee, B.C. Wei, T.H. Zhang, Y.Z. He, Mat. Sci. Eng. a-Struct. 478 (1–2) (2008) 371–375.
[47] B.C. Wei, T.H. Zhang, W.H. Li, D.M. Xing, L.C. Zhang, Y.R. Wang, Mater. Trans. 46 (12) (2005) 2959–2962.
[48] S. Yang, Y.W. Zhang, K.Y. Zeng, J. Appl. Phys. 95 (7) (2004) 3655–3666.
[49] A.H.W. Ngan, B. Tang, J. Mater. Res. 17 (10) (2002) 2604–2610.
[50] J.L. Wu, Y. Pan, J.H. Pi, Appl. Phys. a-Mater. 115 (1) (2014) 305–312.
[51] X.Y. Wang, P. Gong, L. Deng, J.S. Jin, S.B. Wang, P. Zhou, J. Non Cryst. Solids 470 (2017) 27–37.
[52] L.C. Zhang, B.C. Wei, D.M. Xing, T.H. Zhang, W.H. Li, Y. Liu, Intermetallics 15 (5–6) (2007) 791–795.
[53] K.M. Bernatz, I. Echeverria, S.L. Simon, D.J. Plazek, J. Non Cryst. Solids 307 (2002) 790–801.
[54] V. Ocelík, K. Csach, A. Kasardová, V.Z. Bengus, Mater. Sci. Engi. 226-228 (1997) 851–855.
[55] A. Inoue, A. Takeuchi, Acta Mater. 59 (6) (2011) 2243–2267.
[56] W.L. Johnson, MRS Bull. 24 (10) (1999) 42–56.
[57] C.A. Schuh, T.C. Hufnagel, U. Ramamurty, Acta Mater. 55 (12) (2007) 4067–4109.
[58] B.A. Sun, S. Pauly, J. Tan, M. Stoica, W.H. Wang, U. Kühn, J. Eckert, Acta Mater. 60 (10) (2012) 4160–4171.
[59] G. Wang, K.C. Chan, L. Xia, P. Yu, J. Shen, W.H. Wang, Acta Mater. 57 (20) (2009) 6146–6155.
[60] D. Klaumunzer, R. Maass, J.F. Loffler, J. Mater. Res. 26 (12) (2011) 1453–1463.
[61] I.-.C. Choi, Y. Zhao, Y.-.J. Kim, B.-.G. Yoo, J.-.Y. Suh, U. Ramamurty, J.-ii. Jang, Acta Mater. 60 (19) (2012) 6862–6868.
[62] X.L. Bian, G. Wang, K.C. Chan, J.L. Ren, Y.L. Gao, Q.J. Zhai, Appl. Phys. Lett. 103 (10) (2013).
[63] M. Zhang, Y.J. Wang, L.H. Dai, J. Non Cryst. Solids 444 (2016) 23–30.
[64] W. Peng, B.C. Wei, T.H. Zhang, Y. Liu, L. Li, Mater. Trans. 48 (7) (2007) 1759–1764.
[65] C.A. Schuh, T.G. Nieh, Acta Mater. 51 (1) (2003) 87–99.
[66] H. Li, A.H.W. Ngan, M.G. Wang, J. Mater. Res. 20 (11) (2005) 3072–3081.
[67] G.K. Liao, Z.L. Long, M.S.Z. Zhao, M. Zhong, W. Liu, W. Chai, J. Non Cryst. Solids 460 (2017) 47–53.
[68] C. Schuh, T.G. Nieh, J. Mater. Res. 19 (2004) 46–57.
[69] H. Chen, Y.X. Song, T.H. Zhang, M. Wu, Y. Ma, J. Non Cryst. Solids 499 (2018) 257–263.
[70] W.C. Oliver, G.M. Pharr, J. Mater. Res. 7 (6) (1992) 1564–1583.
[71] Y.M. Lu, B.A. Sun, L.Z. Zhao, W.H. Wang, M.X. Pan, C.T. Liu, Y. Yang, Sci. Rep. 6 (2016).
[72] C. Schuh, A. Lund, J. Mater. Res. 19 (2004) 2152–2158.
[73] D. Tonnies, K. Samwer, P.M. Derlet, C.A. Volkert, R. Maass, Appl. Phys. Lett. 106 (17) (2015).
[74] H. Guo, C.B. Jiang, B.J. Yang, J.Q. Wang, J. Mater. Sci. Technol. 33 (11) (2017) 1272–1277.
[75] J.D. Bernal, Nature 183 (4655) (1959) 141–147.
[76] Y. Ma, J.H. Ye, G.J. Peng, D.H. Wen, T.H. Zhang, Mater. Sci. Eng. 627 (2015) 153–160.
[77] P. Huang, F. Wang, M. Xu, K.W. Xu, T.J. Lu, Acta Mater. 58 (15) (2010) 5196–5205.
[78] I.C. Choi, B.G. Yoo, Y.J. Kim, J.I. Jang, J. Mater. Res. 27 (1) (2012) 2–10.
[79] F. Wang, J.M. Li, P. Huang, W.L. Wang, T.J. Lu, K.W. Xu, Intermetallics 38 (2013) 156–160.
[80] M. Heggen, F. Spaepen, M. Feuerbacher, J. Appl. Phys. 97 (3) (2005).
[81] L.S. Luo, B.B. Wang, F.Y. Dong, Y.Q. Su, E.Y. Guo, Y.J. Xu, M.Y. Wang, L. Wang, J.X. Yu, R.O. Ritchie, J.J. Guo, H.Z. Fu, Acta Mater. 171 (2019) 216–230.
[82] Y.Q. Su, F.Y. Dong, L.S. Luo, J.J. Guo, B.S. Han, Z.X. Li, B.Y. Wang, H.Z. Fu, J. Non Cryst. Solids 358 (18–19) (2012) 2606–2611.
[83] J.A. Rodriguez, D.W. Goodman, Science 257 (5072) (1992) 897.
[84] R.A. Oriani, P.H. Josephic, Scripta Metallurgica 6 (8) (1972) 681–688.
[85] A.R. Troiano, Metal., Microstruct. Anal. 5 (6) (2016) 557–569.
[86] D. Setoyama, J. Matsunaga, H. Muta, M. Uno, S. Yamanaka, J. Alloys Compd. 385 (1) (2004) 156–159.